



N₂O decomposition over CuO/CeO₂ catalyst: New insights into reaction mechanism and inhibiting action of H₂O and NO by *operando* techniques

Maxim Zabitskiy^a, Petar Djinoić^a, Elena Tchernychova^b, Albin Pintar^{a,*}

^a Laboratory for Environmental Sciences and Engineering, National Institute of Chemistry, Hajdrihova 19, SI-1001 Ljubljana, Slovenia

^b Laboratory for Materials Chemistry, National Institute of Chemistry, Hajdrihova 19, SI-1001 Ljubljana, Slovenia

ARTICLE INFO

Article history:

Received 27 November 2015

Received in revised form 4 February 2016

Accepted 8 February 2016

Available online 11 February 2016

Keywords:

N₂O decomposition

CuO/CeO₂ nanorods catalyst

Operando DR UV–vis

In situ DRIFTS

Reaction mechanism

ABSTRACT

In this work, a combination of *ex situ* (STEM-EELS, STEM-EDX, H₂-TPR and XPS), *in situ* (CO-DRIFTS) and *operando* (DR UV–vis and DRIFTS) approaches was used to probe the active sites and determine the mechanism of N₂O decomposition over highly active 4 wt.% Cu/CeO₂ catalyst. In addition, reaction pathways of catalyst deactivation in the presence of NO and H₂O were identified. The results of *operando* DR UV–vis spectroscopic tests suggest that [Cu–O–Cu]²⁺ sites play a crucial role in catalytic N₂O decomposition pathway. Due to exposure of {100} and {110} high-energy surface planes, nanorod-shaped CeO₂ support simultaneously exhibits enhancement of CuO/CeO₂ redox properties through the presence of Ce³⁺/Ce⁴⁺ redox pair. Its dominant role of binuclear Cu⁺ site regeneration through the recombination and desorption of molecular oxygen is accompanied by its minor active participation in direct N₂O decomposition. NO and H₂O have completely different inhibiting action on the N₂O decomposition reaction. Water molecules strongly and dissociatively bind to oxygen vacancy sites of CeO₂ and block further oxygen transfer as well as regeneration of catalyst active sites. On the other hand, the effect of NO is expressed through competitive oxidation to NO₂, which consumes labile oxygen from CeO₂ and decelerates [Cu⁺ Cu⁺] active site regeneration.

© 2016 Elsevier B.V. All rights reserved.

1. Introduction

Nitrous oxide (N₂O) is due to its high global warming potential, atmospheric stability (lifetime approximately 120 years) and contribution to ozone layer depletion considered to be one of the strongest greenhouse gases [1,2]. The total anthropogenic emissions of nitrous oxide (including nitric acid, adipic acid and caprolactam production) are estimated to be about 5.3 Tg N₂O–N yr^{−1} (teragrams of N₂O in equivalent nitrogen units per year) [3]. Thus, development of an efficient technology for catalytic N₂O decomposition from industrial exhaust gases is highly required. Different catalyst formulations (involving supported noble metals [4–6], metal oxides [7,8], mixed metal oxides [9,10], perovskites [11,12], spinels [13–15] and zeolite based materials [16–19]) have been studied in order to decompose N₂O to environmentally benign O₂ and N₂. Despite many scientific efforts, development of a proper catalyst which could decompose N₂O even

in the presence of inhibiting gases (e.g., water, oxygen and NO) is still of great importance.

Among investigated catalytic systems, CuO/CeO₂ materials show very promising results and combine superior activity under moderate temperatures, long-term stability and economically favourable price (compared to highly expensive noble metals) [10,20–23]. It was previously discovered that CuO clusters measuring less than 5 nm in size exhibit the highest activity and achieve 50% of N₂O conversion at around 380 °C (N₂O concentration = 2500 ppm; WHSV = 60 L/(g_{cat} h)) [21]. Exceptional catalytic properties of CuO/CeO₂ system have been attributed to the so-called “synergetic effect”. This originates from electronic interactions between the two oxide phases, which weakens the metal-oxygen bond and enables easier oxygen desorption and regeneration of catalyst active sites [24,25]. It was observed that nanoshaped CeO₂ (rods and cubes), predominantly terminated with {100} and {110} surface planes and enriched with Ce³⁺ showed superior activity in N₂O decomposition reaction compared to polycrystalline CeO₂ nanoparticles, terminated with {111} surface planes with lower Ce³⁺ content [20]. This leads to an assumption that CeO₂ acts not only as a support material for CuO,

* Corresponding author.

E-mail address: albin.pintar@ki.si (A. Pintar).

but also plays an active role (through $\text{Ce}^{3+}/\text{Ce}^{4+}$ redox pair) in N_2O decomposition pathway. Systematic fundamental research which would help to identify reaction steps occurring on the catalyst surface during N_2O decomposition, is required in order to establish a credible mechanism for catalytic N_2O decomposition over CuO/CeO_2 solids. Furthermore, the inhibiting action of H_2O and NO , which are usually present in tail gases subjected to N_2O decomposition, is not completely clear.

As a result, understanding of N_2O decomposition mechanism and deactivation by H_2O and NO will allow catalyst improvement for efficient N_2O destruction. Therefore, this study was aimed to fulfil this missing knowledge gap. For this purpose, a catalyst containing 4 wt.% of Cu supported on CeO_2 nanorods was thoroughly characterized by a variety of techniques (HRTEM, STEM-HAADF, STEM-EDX, N_2 physisorption, XRD, H_2 -TPR, XPS and dissociative N_2O adsorption) and examined in catalytic N_2O decomposition. *Operando* DRIFT and UV–vis techniques hyphenated with gas chromatography were used to investigate the mechanism of N_2O decomposition over CuO/CeO_2 as well as inhibiting action of H_2O and NO on the catalyst. By bringing together results obtained from these surface sensitive techniques, comprehensive information about the reaction under consideration was obtained and mechanism of catalytic N_2O decomposition was proposed.

2. Experimental

2.1. Catalyst preparation

Catalyst containing 4 wt.% of Cu supported on CeO_2 nanorods (CuO/CeO_2) was prepared accordingly to the following synthesis protocol: Nanoshaped CeO_2 support was synthesized by hydrothermal method. Briefly, 53.8 g of NaOH (99% purity, Merck) was dissolved in 140 mL of deionized water. To the obtained solution, 4.9 g of $\text{Ce}(\text{NO}_3)_3 \cdot 6\text{H}_2\text{O}$ (99% purity, Sigma-Aldrich) dissolved in 84 mL of deionized water was added under vigorous stirring. Then, suspension was stirred for 30 min and transferred into a Teflon[®]-lined stainless steel autoclave and aged for 24 h at 100 °C. The derived suspensions were centrifuged at 5000 rpm and thoroughly washed with hot deionized water in order to remove undesired sodium ions. The obtained precipitate was re-dispersed in 10 mL of deionized water, frozen by quench-freezing with LN_2 and dried for 24 h using a freeze-dryer (Christ, model Alpha 1–2 LDplus). Finally, the material was calcined in air at 400 °C for 3 h (heating ramp of 2 °C/min). CuO was deposited by means of precipitation. 400 mg of CeO_2 nanorods was dispersed in 10 mL of deionized water using an ultrasonic homogenizer (Cole-Parmer) and 63.6 mg of $\text{Cu}(\text{NO}_3)_2 \cdot 3\text{H}_2\text{O}$ (99.5% purity, Sigma-Aldrich) was added to reach the 4 wt.% nominal loading. After 10 min of stirring, 5 mL of aqueous solution containing 250 mg of Na_2CO_3 (99.999% purity, Merck) was added. The obtained suspension was additionally stirred at room temperature for 2 h, filtered, thoroughly washed with hot deionized water, dried in the freeze drier for 24 h and finally calcined in air at 400 °C for 3 h (heating ramp of 2 °C/min).

2.2. Catalyst characterization

Measurements of BET specific surface area, total pore volume and pore size distribution were performed at –196 °C using a TriStar II 3020 instrument from Micromeritics. Temperature programmed reduction (H_2 -TPR) experiments were performed using a Micromeritics AutoChem II 2920 apparatus. Before analysis, a catalyst was pre-treated at 400 °C in synthetic air (20.5 vol.% O_2/N_2). TPR analysis was performed in a 25 mL/min stream of 5 vol.% H_2/Ar mixture as a reducing agent. The samples were heated from –20 to 400 °C with a 5 °C/min ramp during analysis. A liquid

nitrogen–isopropyl alcohol cold trap was mounted on exhaust in order to condense water vapour and remove it from the effluent gas mixture before entering the TCD detector. After H_2 -TPR examination, dissociative N_2O adsorption experiment was done in order to determine Cu dispersion and cluster size. N_2O pulsing (10 vol.% $\text{N}_2\text{O}/\text{He}$) was performed at 35 °C (a LN_2 cold trap was mounted on exhaust in order to condense unreacted N_2O). X-ray photoelectron spectra were measured with ES-2403 modified spectrometer equipped with a PHOIBOS 100 MCD analyzer (Specs GmbH), using $\text{MgK}\alpha$ excitation (1253.6 eV, 10 kV and 25 mA). The spectrometer was calibrated by binding energy (BE) of $\text{Au } 4f_{7/2} = 84.0$ eV and $\text{Ni } 2p_{3/2} = 852.7$ eV. Detailed spectra were recorded for the regions of Cu 2p, Ce 3d photoelectrons and Cu L3VV Auger electrons with a 0.1 eV step at a pressure below 3×10^{-6} Pa. The binding energy of XPS peaks was further corrected by referencing to the Ce $3d_{5/2}$ peak at 882.0 eV (internal standards). Particle size and morphology were studied by means of high-resolution transmission electron microscopy (HRTEM) and scanning TEM high-angle annular dark field imaging (STEM-HAADF). Copper distribution was assessed by energy-dispersive X-ray spectroscopy in STEM mode (STEM-EDX). For these analyses, a probe aberration-corrected JEM-ARM200CF equipped with the JEOL Centurio 100 mm² EDXS detector and JEOL STEM detectors (JEOL, Tokyo, Japan) was employed.

2.3. In situ and operando experiments

All experiments were carried out at ambient pressure. Prior to catalytic runs, the CuO/CeO_2 catalyst was activated *in situ* in 20 mL/min Ar flow (purity 5.0, Messer) at 400 °C for 1 h. Decomposition of N_2O was performed in reaction chambers (see details below) in the temperature range of 300–450 °C. N_2O feed concentration was 2500 ppm balanced by argon (Linde), while the total feed flow rate was equal to 30 mL/min. At each examined temperature (increments of 50 °C) the reaction was carried out for 30 min before measurements were initiated. For catalytic experiments conducted in the inhibiting atmospheres, gas mixtures containing 2500 ppm of N_2O and either 1.5 vol.% of H_2O or NO balanced by argon were used.

The *operando* diffuse reflectance Fourier transform infrared (DRIFT) spectra were recorded in the range of 900–4000 cm^{-1} using a FTIR analyzer (Perkin Elmer, model Frontier) equipped with a MCT detector. High temperature reaction chamber (Pike Technologies, model DiffusIR) was used in order to monitor the catalyst surface under reaction conditions. Experiments were conducted using 10 mg of CuO/CeO_2 sample placed into a sample holder made from sintered ceramics (5 mm I.D.) and finely smoothed to create a flat surface. Spectra were collected with the resolution of 4 cm^{-1} and accumulation of 32 scans. The analysis of outlet gas was performed by means of a hyphenated gas chromatograph 490 Micro GC (Agilent Technologies) equipped with 10 m MS5A and 10 m Porabond Q columns. *In situ* spectra of adsorbed CO were recorded at –70 °C. The catalyst was pre-treated *in situ* either in inert gas (He) or in 2500 ppm $\text{N}_2\text{O}/\text{Ar}$ atmospheres at 400 °C. After cooling to –70 °C, the solid was exposed to 1 vol.% CO/Ar mixture. Spectra were collected with the resolution of 4 cm^{-1} and accumulation of 16 scans.

The *operando* UV–vis diffuse reflectance spectra (DR UV–vis) were acquired using a Perkin-Elmer Lambda 650 UV–vis spectrophotometer equipped with a high-temperature reaction chamber (HVC-VUV-4, Harrick). The Spectralon[®] white reflectance standard or CuO/CeO_2 catalyst were utilized to perform the instrument background correction in the range of 200–850 nm. The scans were acquired with the speed of 120 nm min^{-1} and slit set to 4 nm. 10 mg of CuO/CeO_2 catalyst was placed into a stainless steel sample holder (4.5 mm I.D.) inside the reaction chamber. N_2O conversion

was monitored by using the hyphenated gas chromatograph (Agilent, model 490 Micro GC).

3. Results and discussion

3.1. Ex situ catalyst characterization

Selection of 4 wt.% of Cu supported on CeO₂ nanorods catalyst ($S_{\text{BET}} = 82 \text{ m}^2/\text{g}$) for *operando* mechanism investigation was based on results of our previous study, where among tested solids (2–8 wt.% Cu deposited over differently nanoshaped CeO₂ supports) this material showed the highest activity in N₂O decomposition reaction and significantly exceeded the catalytic properties of pure CuO and CeO₂ phases (Fig. S1) due to synergetic effect [20]. Accordingly to STEM-HAADF image (Fig. 1a) the catalyst consists of nanorods being between 80 and 140 nm in length and 8 nm in width. Interplanar spacings of 0.27 and 0.19 nm were determined from the HRTEM images (not shown), which corresponds to {100} and {110} exposed surface planes of CeO₂. No CuO particles could be identified directly from the contrast differences in STEM-HAADF images; therefore, STEM-EDX analysis was further performed (Fig. 1b and c). It was found that CuO phase is finely dispersed over CeO₂ nanorods and CuO particles size varied from 1.5 to 5 nm. These results were further confirmed by means of dissociative N₂O chemisorption experiment, where 46% of Cu dispersion was observed that corresponds to 2.4 nm average CuO particle size. Due to (i) high CuO dispersion resulting in increased synergetic interaction between CuO phase and CeO₂ support, and (ii) exposed {100} and {110} high-energy surface planes, enhancement of CuO/CeO₂ redox properties was revealed. Primarily this is expressed in lower activation energy for oxygen desorption, formation of oxygen vacancies and enrichment of catalyst surface with reduced Ce³⁺ and Cu⁺ oxidation states, as confirmed by H₂-TPR, XPS and STEM-EELS examinations.

According to H₂-TPR analysis, reduction profile of CuO/CeO₂ catalyst is significantly shifted to lower temperatures compared to those of individual CuO and CeO₂ components (Fig. S2). By quantification of H₂ consumed during the H₂-TPR test (this amount considerably surpassed the theoretical values, required for complete reduction of Cu²⁺ to Cu⁰) not only reduction of CuO phase, but also co-reduction of CeO₂ support was verified. Furthermore, by using X-ray photoelectron spectroscopy technique it was found that Ce 3d core-level XPS spectra contain both Ce⁴⁺ and Ce³⁺ oxidation states (Fig. S3a). Additionally, O1s spectrum (Fig. S3b) contains besides the main peak at 529.1 eV also a shoulder at 531.3 which was previously attributed to highly polarized oxide ions located closely to the anion defect sites (oxygen vacancies) with nearby low coordinated Ce⁴⁺ [26,27]. This confirms that both oxygen desorption and formation of oxygen vacancies take place under experimental conditions (ambient temperature, ultra-high vacuum). After baseline subtraction and peak deconvolution with symmetric Gaussian-Lorentzian functions (see Fig. S3a and Table S1), it was calculated that 41% of Ce is present in Ce³⁺ oxidation state within the probing depth of XPS analysis, which is about 1 nm and corresponds to 2CeO₂ unit cell sizes. At the same time, shake-up satellites at higher apparent Cu 2p_{3/2} binding energy were absent, indicating that Cu is also present in the reduced state. Position of the Auger Cu L₃VV electron line (916.1 eV) as well as the modified Auger parameter (1848.7 eV) indicate the presence of Cu⁺ species on the catalyst surface. Results of *in situ* DRIFTS CO chemisorption analysis also confirmed reduced state of copper. As one can see from temperature resolved spectra (Fig. S4), at least four absorption peaks are present with maxima at 2142, 2109, 2101 and 2058 cm⁻¹. These vibration bands could be assigned to Cu⁺ (2142, 2109 and 2101 cm⁻¹) and Cu⁰ (2058 cm⁻¹) surface sites, whereas detailed

discussion regarding attribution of these peaks can be found in our previous study [20].

In addition to H₂-TPR and XPS examinations, STEM-EELS analysis provided further information about the changes in the oxidation state of Ce ions as a function of their distance from the nanorod surface. The spectra acquisition parameters (accelerating voltage, acquisition time, probe current) were thoroughly tuned in order to minimize electron beam damage of CeO₂.

STEM-HAADF image of the catalyst under examination with an EELS line profile position is shown in Fig. 2a. Points 1, 2 and 3 denote the positions where the spectra of Ce M_{4,5} edge presented in Fig. 2b were acquired. Due to differences in positions and shapes of Ce M_{4,5} edges belonging to Ce⁴⁺ and Ce³⁺, these two valence states could be distinguished by EELS. The 1.25 eV shift towards higher energy of the Ce M_{4,5} edge maxima (denoted with letters a and c) as well as a change of their intensities were observed for the spectrum acquired at point 3 (Fig. 2b). Furthermore, the secondary maxima characteristic for Ce⁴⁺ ELNES structure of the Ce M_{4,5} edge (Fig. 2b, maxima denoted with b and d) are absent in the spectrum at the point 1. They appear most prominently in the spectrum 3, which was recorded close to the nanorod's centre. These results expose the enrichment of the CeO₂ nanorod surface layers with Ce³⁺ oxidation state. The depth of the Ce³⁺ shell was determined by using modified integral Ce M_{4,5} white-line intensity ratio [28], calculated for each spectrum of the line scan analysis and plotted as a function of the distance from the CeO₂ surface (Fig. 2c). A continuous drop of the Ce³⁺/Ce⁴⁺ intensity ratio until about 1.6 nm distance from the nanorod's surface is seen. This corresponds to the gradual change from Ce³⁺ to Ce⁴⁺ oxidation state along this distance, which was also observed through the characteristic changes in the ELNES of the Ce M_{4,5} edge spectra. Abovementioned results reveal enrichment of CeO₂ nanorod's surface with Ce in 3+ oxidation state, while bulk of the nanorod consists mostly of Ce⁴⁺. The observed results are in good agreement with the findings of XPS study, where ceria surface is highly enriched with Ce³⁺ oxidation state.

Based on data obtained from *ex situ* characterization techniques, we can set the following grounds prior to employing *in situ* and *operando* techniques. Synergetic interaction between CuO and CeO₂ oxide phases results in enhanced redox properties of this solid, easier oxygen desorption and enrichment of catalyst surface with reduced Cu⁺ and Ce³⁺ states. Therefore, both Cu⁺/Cu²⁺ and/or Ce³⁺/Ce⁴⁺ ionic pairs can contribute as active sites in individual catalytic steps of N₂O decomposition. In order to determine and prove the real active sites and catalytic mechanism of N₂O degradation, *in situ* and *operando* measurements are crucial.

3.2. In situ and operando N₂O decomposition

Prior to catalytic N₂O decomposition, the CuO/CeO₂ material was activated in Ar at 400 °C for 1 h. In order to reveal surface changes of the catalyst during this process and to find the relevant reference point before catalytic runs, pre-treatment of CuO/CeO₂ catalyst in inert atmosphere was studied by *in situ* DRIFTS and DR UV-vis techniques. Fig. S5 presents the DRIFT spectra of CuO/CeO₂ material acquired at different temperatures during catalyst activation (heating ramp of 10 °C/min). During thermal treatment (catalyst activation), water desorption accompanied by dehydroxylation of the catalyst surface takes place (mainly below 250 °C), which results in disappearance of a broad peak between 3000 and 3700 cm⁻¹. Absorption peaks at 3502 and 3642 cm⁻¹ corresponding to bridged hydroxyl and polydentate hydroxyl groups with acid character on ceria surface [29] are present in the DRIFT spectrum even after 1 h at 400 °C. Thermal stability of abovementioned hydroxyl groups was confirmed by works of Soria et al. [29] and Binet et al. [30]. Other significant changes were not observed during *in situ* DRIFTS catalyst activation.

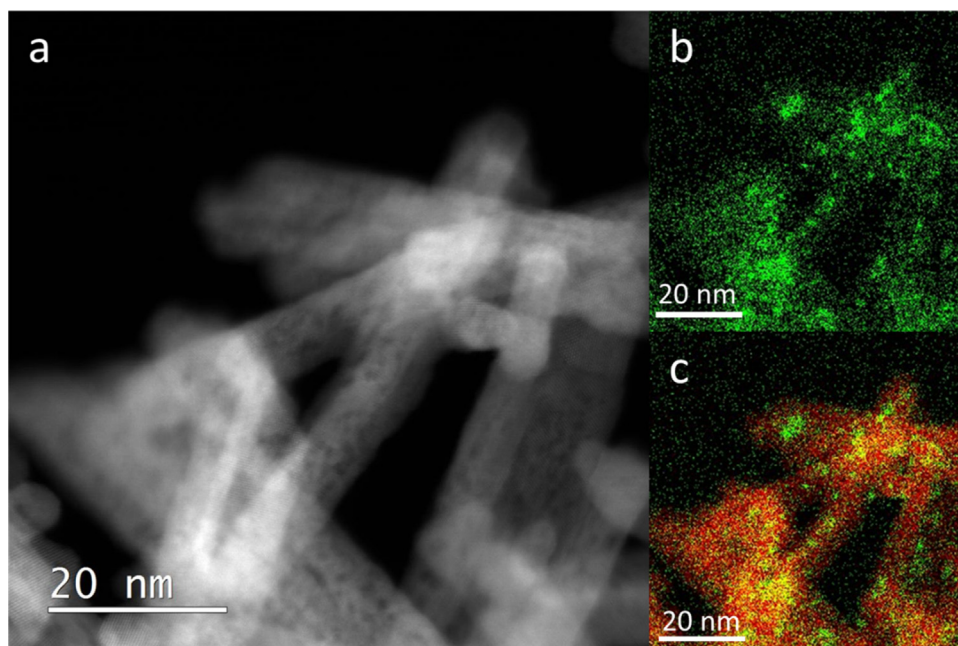


Fig. 1. HAADF-STEM micrograph of CuO/CeO₂ catalyst (a), EDX elemental mapping of Cu (b) and EDX elemental mapping overlay of Ce and Cu (c).

Additional information regarding changes of the catalyst during activation was obtained by *in situ* DR UV–vis spectroscopy. During heating from 30 to 150 °C, d–d transition band of Cu²⁺ shifted from 780 to 700 nm and became more intensive (Fig. S6a). Generally, absorption between 600 and 800 nm is attributed to d–d transition of Cu²⁺ in an octahedral configuration with tetragonal distortion. With increasing extent of distortion, the wavelength progressively decreases. In the case of strong tetragonal distortion (nearly square planar configuration of Cu²⁺) position of the absorption peak could be at around 600 nm, while Cu²⁺ in perfect O_h symmetry absorbs at 800 nm [31,32]. Taking into account results of *in situ* DRIFT examination, we propose that during the thermal treatment configuration of surface Cu²⁺ changes from initial octa-

hedral to tetragonal distorted O_h symmetry due to dehydroxylation and formation of surface Cu²⁺ defect sites.

Further heating to 400 °C resulted in a gradual increase of two absorption peaks centered at 428 and 576 nm, which can be well visualized on difference DR UV–vis spectra (Fig. S6b). The peak with a maximum at 428 nm was previously ascribed to an O → Cu charge transfer transition of a bis(μ-oxo) dicopper complex [33]. However, recent studies based on resonance Raman spectroscopy in combination with DFT calculations gave an evidence that this band can be uniquely defined as a bent mono(oxo) dicopper site [Cu–O–Cu]²⁺ [34,35]. Taking into account previously discussed results of *in situ* DRIFTS examination, where extensive dehydroxylation of the cat-

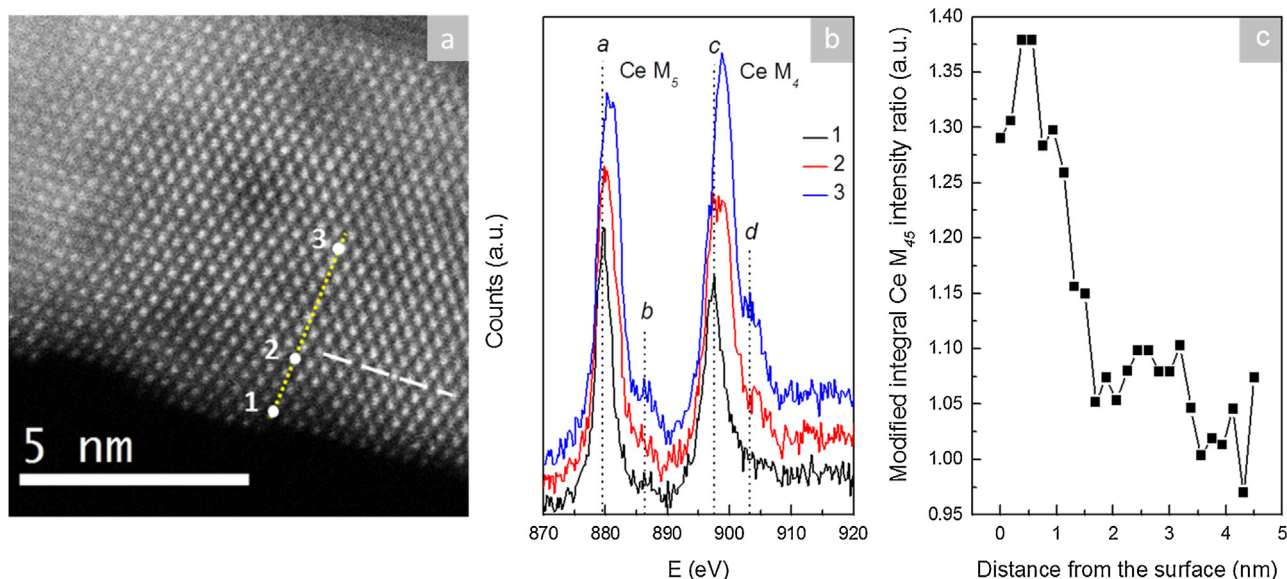
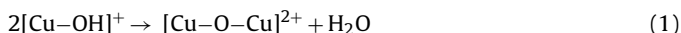
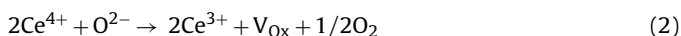


Fig. 2. (a) STEM-HAADF image of CuO/CeO₂ catalyst with the yellow dotted line showing the position of the EELS line scan and white dashed line showing the region with predominant Ce³⁺. Points 1–3 correspond to the extracted spectra of Ce M₄₅ edge shown in (b), where letters a, b, c and d denote peak positions shown by dotted lines. In (c) the modified integral Ce M₄₅ edge intensity ratio derived from the line scan spectra is plotted versus distance from the surface of CeO₂ nanorod. (For interpretation of the references to color in this figure legend, the reader is referred to the web version of this article.)

alyst surface was observed, formation of $[\text{Cu}-\text{O}-\text{Cu}]^{2+}$ sites could be expressed by the following equation (Eq. (1)):



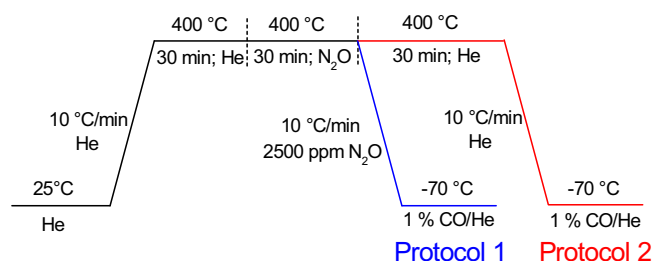
At the same time, growth of absorption band with a maximum at 576 nm could be attributed to surface reduction of CeO_2 . Binet et al. [30] performed reduction of CeO_2 by H_2 combined with *in situ* spectroscopic characterization. They have observed an electronic defect transition at 588 nm and ascribed it to Ce^{3+} – Ce^{4+} charge transfer. Nottbohm et al. [36] have investigated CeO_2 by Raman, UV–vis and X-ray photoelectron spectroscopy combined in one experimental setup. They observed a broad absorption peak at around 500 nm after exposure of CeO_2 to X-rays and attributed this band to surface and bulk CeO_2 reduction. In order to confirm assignment of peak at 576 nm to Ce^{3+} – Ce^{4+} charge transfer as a result of CeO_2 reduction (formation of oxygen vacancies and Ce^{3+} surface sites), *in situ* DR UV–vis measurements of CeO_2 support activated in Ar at different temperatures was conducted (Fig. S7). At temperatures above 300 °C a broad absorption band with a maximum at around 585 nm was observed, with a simultaneous change of CeO_2 powder colour from pale yellow to orange. Therefore, we can conclude that the peak centered at 576 nm in CuO/CeO_2 sample originates from CeO_2 phase and is most probably due to Ce^{3+} – Ce^{4+} charge transfer as a result of Ce^{3+} surface site formation. The process occurring on the catalyst surface which is related to the appearance of peak at 576 nm, could be expressed by the following reaction (Eq. (2)), where besides reduction of CeO_2 evolution of gaseous oxygen and formation of anion vacancy take place:



After catalyst activation in Ar flow, the feed gas composition was switched to 2500 ppm $\text{N}_2\text{O}/\text{Ar}$ and catalytic N_2O decomposition was studied. Concentration profiles of N_2O , N_2 and O_2 obtained during the first hour of operation are presented in Fig. S8. Initial period of time is characterized by almost complete N_2O conversion and liberation of a stoichiometric amount of N_2 . At the same time O_2 was not observed in the gas mixture. After 10 min time on stream, O_2 concentration profile began to grow, while N_2O conversion and evolution of N_2 decreased. Finally, all three curves stabilized at steady-state levels after 30 min time on stream. High N_2O conversion in the initial 10 min of reaction, together with the lack of O_2 in the reactor outlet suggest that during this time span, the catalyst was oxidized to a stable working state.

Results of *operando* DR UV–vis examination (Fig. S9) help to shed light on changes occurring in the catalyst state during the initial 30 min time period of catalytic N_2O decomposition. Presence of N_2O in the feed gas affects both copper and cerium oxidation states. Difference spectra (Fig. S9b) show higher reflectance for peaks with maxima at 440 and 572 nm and lower reflectance in the range of d–d Cu^{2+} transition (746 nm). The catalyst changes caused by the presence of N_2O were reflected in the lowering of amount of reduced Ce^{3+} sites (peak at 572 nm), while the concentration of Cu^{2+} was increasing. Previously, it was reported that N_2O can titrate not only reduced Cu, but also oxygen vacancies in a non-stoichiometric support [37]. Taking into account the absence of gaseous O_2 and very high N_2O conversion in the initial minutes, we believe that oxidation of Ce^{3+} and Cu^+ sites took place until catalyst reached an equilibrium concentration of oxygen vacancies. By prolonging the time on stream, decomposition of N_2O resulted in both O_2 and N_2 evolution as a result of the catalyst achieving the steady state determined by the reaction conditions employed in the study.

In order to identify the sites which are active in N_2O decomposition reaction, *operando* DR UV–vis spectra (Fig. 3a) were collected under relevant reaction temperatures (300–450 °C). N_2O conversion in this temperature range increased from 3 to 31% and by comparing catalytic results with the acquired spectroscopic data,



Scheme 1. Catalyst treatments before CO chemisorption experiments.

we can identify the sites which are likely involved in the catalytic pathway. Fig. 3b reveals changes in difference DR UV–vis spectra (spectrum at 300 °C was subtracted from spectra recorded at higher temperatures), which could be attributed to the presence of Ce^{3+} sites (maximum at 589 nm) and bent mono(oxo) dicopper site $[\text{Cu}-\text{O}-\text{Cu}]^{2+}$ (maximum at 422 nm). The higher the catalytic activity (and temperature) were, the lower reflectance was observed for abovementioned bands. This indicates an increase of concentration of both reduced Ce^{3+} and mono(oxo) dicopper sites at higher N_2O conversions. It was reported previously that $[\text{Cu}-\text{O}-\text{Cu}]^{2+}$ species are active in catalytic N_2O degradation over Cu-ZSM-5 [35], while tentative involvement of $\text{Ce}^{3+}/\text{Ce}^{4+}$ redox pair in catalytic mechanism was proposed for CuO/CeO_2 solids [21,23].

In order to probe surface Cu oxidation state under different reaction atmospheres, *in situ* DRIFTS of CO chemisorbed at –70 °C examinations were conducted. Experiments were carried out in such a manner that allowed testing a catalyst, which has been subjected either to 2500 ppm $\text{N}_2\text{O}/\text{Ar}$ (protocol 1) or He atmosphere (protocol 2) at 400 °C prior to CO chemisorption (Scheme 1).

Fig. 4 presents DRIFTS data collected after abovementioned pre-treatments in 0.5 min increments. Intensity of bands increased by prolonging the CO exposure time. Main differences in the spectra of CuO/CeO_2 sample were observed in the region, where vibrations of carbonate groups appear. When the CuO/CeO_2 material was subjected to protocol 1, a significant growth of vibration bands at 1610, 1575, 1277 and 1007 cm^{-1} was observed after CO adsorption. On the other hand, after protocol 2 was carried out, the peaks belonging to carbonates were less intensive. Accordingly to the literature, these peaks are usually attributed to bidentate carbonate species [38,39] on ceria. At the same time, bands with maxima at 2177 and 2156 cm^{-1} were more intensive for the catalyst exposed to protocol 2. The same sharp bands at 2172 and 2156 cm^{-1} were found during CO adsorption at –183 °C on Au/CeO_2 catalyst [40] and were attributed to CO adsorbed onto two kinds of Ce^{4+} sites with different coordinative unsaturation. Binet et al. [41] assigned these peaks to Ce^{4+} carbonyls during IR study of CO adsorption on polycrystalline CeO_2 .

Formation of carbonate group from chemisorbed CO is possible only after chemical bond rearrangement which involves two labile oxygen atoms, located adjacent to the surface site responsible for CO chemisorption. During transient behaviour of CuO/CeO_2 catalyst at temperatures below 300 °C, N_2O is catalytically decomposed, but only N_2 evolution takes place. This is due to a low rate of O_2 recombination and desorption, resulting in oxygen remaining on the catalyst surface. When all available oxygen sites (anion vacancies) are occupied, further N_2O degradation is not possible. Intensive bands ascribed to bidentate carbonate species on CeO_2 after catalyst exposure to protocol 1 provide evidence that the labile oxygen atoms, which originate from the catalytic N_2O decomposition and are involved in oxidation of chemisorbed CO, most likely reside on CeO_2 support. The fact that bands of Ce^{4+} carbonyls are less intensive for the catalyst exposed to protocol 1 also confirms the abovementioned hypothesis. This occurs due to oxidation of

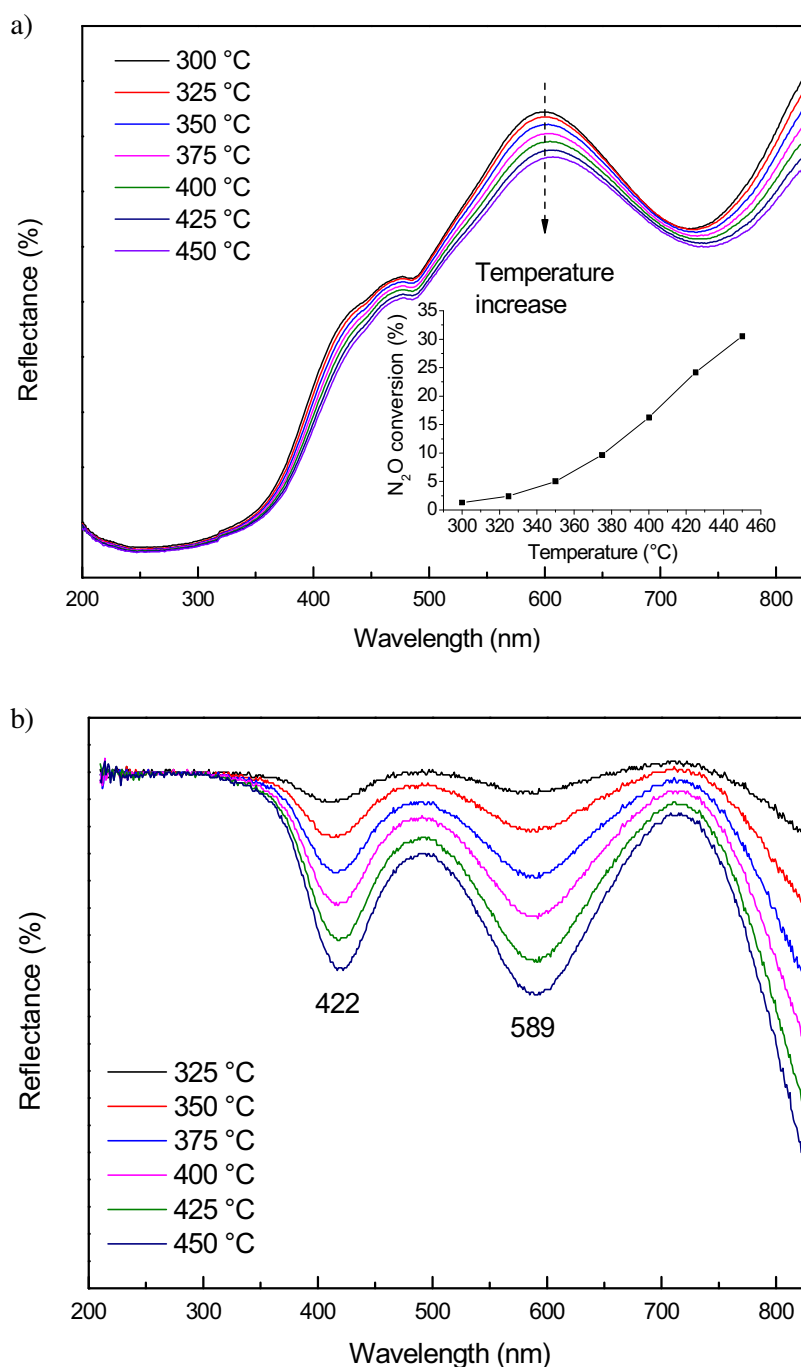


Fig. 3. Operando DR UV-vis spectra (a) of CuO/CeO₂ catalyst during N₂O decomposition at different temperatures (inset shows N₂O conversion profile), and (b) difference DR UV-vis spectra which were obtained by subtraction of spectrum at 300 °C from other spectra.

surface carbonyls (formed after CO adsorption on Ce⁴⁺ sites) with labile oxygen, resulting in lower intensity of their corresponding bands at 2177 and 2157 cm⁻¹.

Besides their intensity, peaks in the Cu carbonyl region of differently pre-treated CuO/CeO₂ catalyst (protocol 1 or protocol 2) do not exhibit noticeable differences. Both spectra contain a main peak at 2100 cm⁻¹ with a shoulder at 2110 cm⁻¹, which are usually assigned to different Cu⁺ sites [20,42]. Additional shoulder with a maximum at 2054 cm⁻¹ could be attributed to Cu⁰ carbonyls [43].

3.3. Inhibition by H₂O and NO: operando study

H₂O and NO are usually present in N₂O-containing gas streams [10,21,22]. They are known to negatively affect catalytic activity of CuO/CeO₂ materials. In order to utilize CuO/CeO₂ solids as potential catalysts for N₂O abatement in industrial sources, the deactivation pathways of H₂O and NO need to be understood. When water vapour was present in the feed gas, N₂O conversion-temperature profiles were shifted to higher temperatures by 70 °C (Fig. S10).

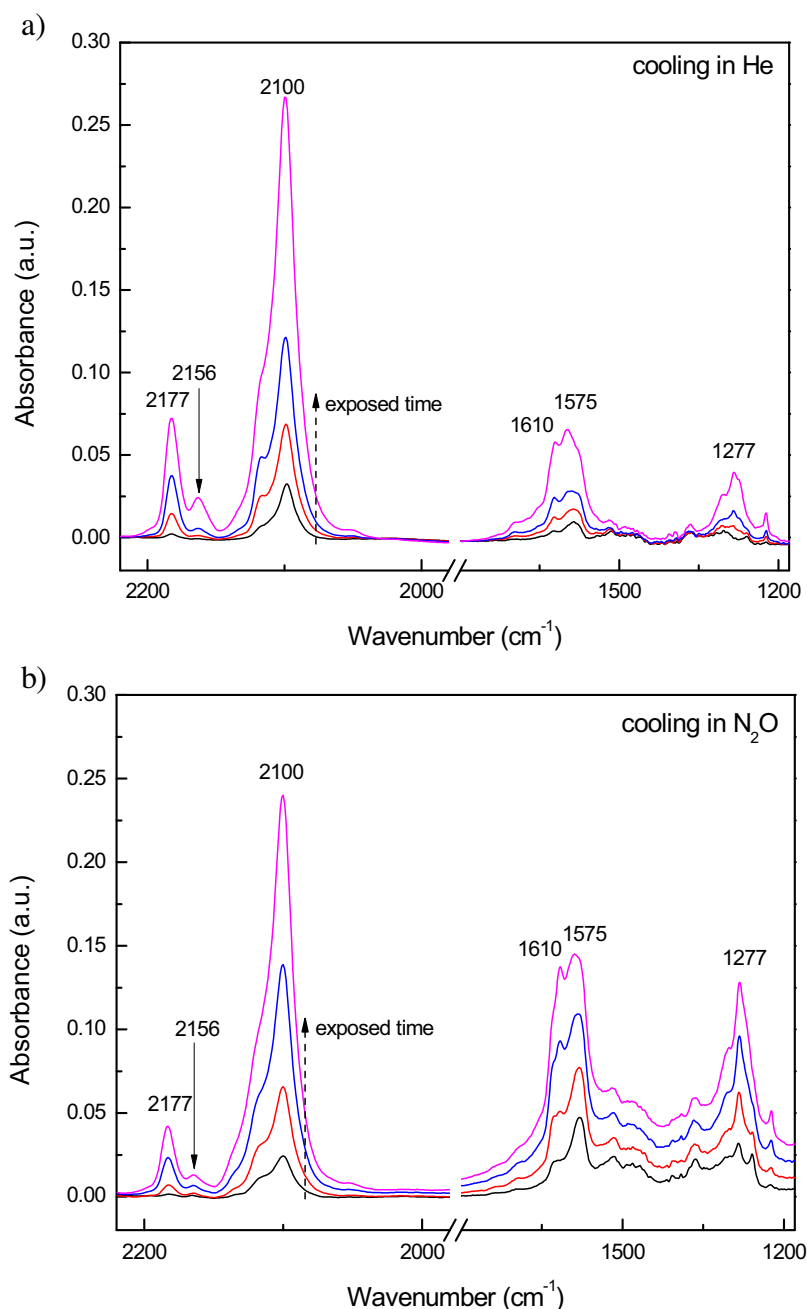


Fig. 4. *In situ* DRIFTS spectra of adsorbed CO at -70°C for CuO/CeO₂ catalyst pre-treated at 400°C and cooled in He (a) and N₂O (b). Spectra were recorded in time increments of 0.5 min.

The negative effect of NO was less pronounced and shifted the conversion-temperature profile by only 10°C .

Results of *operando* DR UV–vis step change experiments (feed gas composition was alternately changed between 2500 ppm N₂O and 2500 ppm N₂O + 1.5% NO) are illustrated in Fig. 5. As could be seen from difference spectra (Fig. 5b), the presence of NO in feed gas composition results in diminution of the peak with a maximum at 624 nm. This band corresponds to d–d transition of Cu²⁺ in an octahedral configuration with tetragonal distortion. Apparently, NO co-feeding resulted in lowering of Cu²⁺ concentration. This process is fully reversible within 30 min, as the DR UV–vis spectrum returned to the initial intensity after elimination of NO from the feed gas stream. *In situ* DRIFTS experiment (Fig. 6) reveals the formation of several bands in the 1000–1600 cm⁻¹ region, when 1.5% NO was present in gas mixture. Bands in this range are attributable

to surface nitrate (NO₃⁻) and nitrito (NO₂⁻) species of different structures [44]. Bands at 1400, 1130 and 1027 cm⁻¹ most likely originate from hyponitrite (N₂O₂⁻) species [45,46], whereas bands at 1545, 1521 and 1222 cm⁻¹ are characteristic either for monodentate nitrate [44] or different structures of nitrito (NO₂⁻) group on surface Cu²⁺ sites [45].

Hyphenated GC-FTIR analysis of gas phase discharged from the reactor after catalytic degradation of 2500 ppm N₂O/1.5% NO/Ar feed revealed the presence of NO₂, complete absence of molecular oxygen as well as N₂ present in an amount that corresponds to the quantity of decomposed N₂O (Fig. S11). Taking into account results of *in situ* DR UV–vis and DRIFTS experiments, as well as absence of O₂ and liberation of NO₂ during catalytic degradation of N₂O in NO containing atmosphere, the following conclusions could be made:

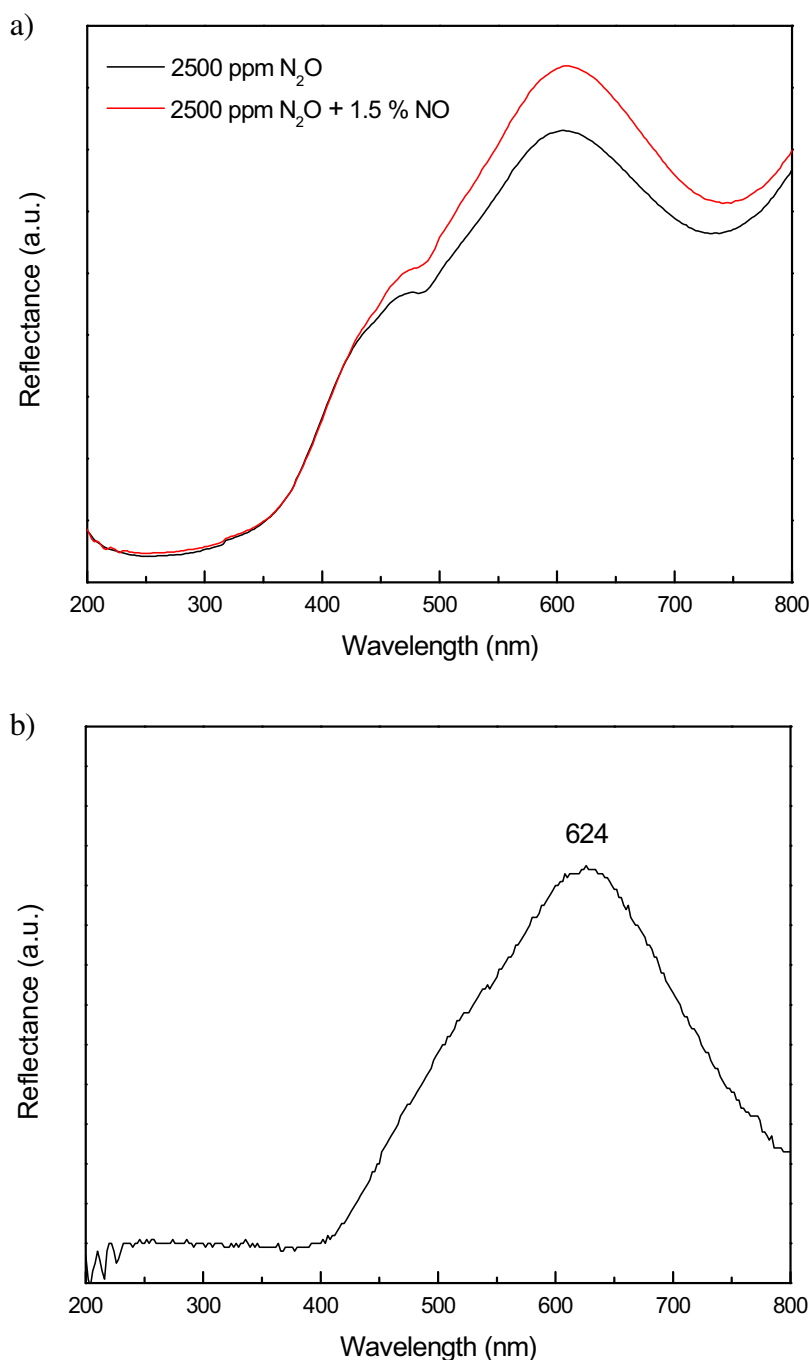
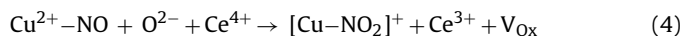


Fig. 5. Operando DR UV-vis spectra (a) of CuO/CeO₂ catalyst during decomposition of 2500 ppm N₂O/1.5% NO/Ar at 400 °C, and (b) difference DR UV-vis spectra obtained by subtraction of spectrum acquired in 2500 ppm N₂O/Ar from other spectra.

- i) Adsorption of NO (Eq. (3)) and further transformation to hyponitrite, nitrite and nitrate species take place on Cu²⁺ sites.
- ii) Nitrite and nitrate groups most probably originate from NO oxidation by labile oxygen species of the catalyst, which originate from N₂O (Eq. (4)).
- iii) Oxidation of NO and formation of nitrito groups is followed by desorption of NO₂ and formation of reduced Cu⁺ state (Eq. (5)).



When N₂O decomposition was inhibited by 1.5 vol.% water vapour, *operando* DR UV-vis step change experiment (Fig. 7) revealed that the amount of mono(oxo) dicopper core (peak at 435 nm) and Ce³⁺ sites (peak at 588 nm) decreased. In turn, results of *in situ* DRIFT spectroscopy (Fig. 8) uncover appearance of peaks and shoulder at 3684, 3642 and 3525 cm⁻¹ as well as broadening in the region of 3500–3000 cm⁻¹. These peaks and shoulder are usually assigned to monodentate, bridged and polydentate hydroxyls groups on CeO₂ surface, respectively [29,30]. Appearance of these hydroxyl species could be explained by dissociative adsorption of H₂O (heterolytic water splitting) on surface oxygen vacancies of ceria according to Eq. (6) [47]. It was confirmed by theoretical calculations that large binding energy of H₂O on the defective sur-

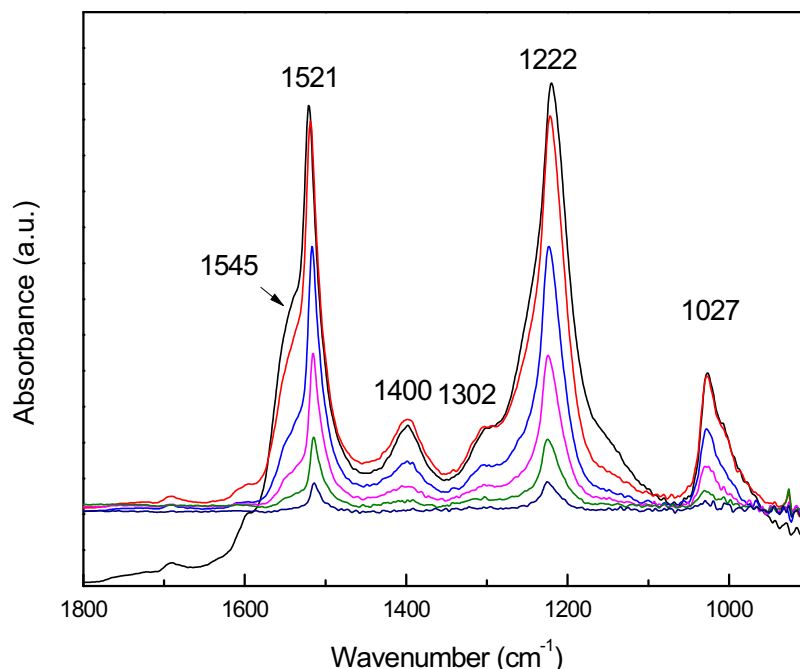


Fig. 6. Operando DRIFTS spectra of CuO/CeO₂ catalyst during decomposition of 2500 ppm N₂O/1.5% NO/Ar at 400 °C.

face sites results in enhanced stability of hydroxyl groups even at temperatures above 400 °C [48]. Besides H₂O dissociation on surface vacancies, H₂ evolution and reoxidation of reduced Ce³⁺ sites through several pathways is also possible [47]. Generally, this process could be expressed by Eq. (7). Duarte et al. [49] have confirmed reoxidation of Ce³⁺ by water at 500 °C by using *in situ* X-ray absorption spectroscopy. Mullins et al. [50] have observed H₂ production at 400 °C during water adsorption on reduced CeO₂. Taking into account results of *operando* DR UV–vis examination (decreasing concentration of Ce³⁺ surface sites was observed), we can conclude that co-feeding of water results in both reoxidation of the catalyst and formation of hydroxyl groups on CeO₂. At the same time, the decreasing amount of mono(oxo) dicopper sites (DR UV–vis peak at 435 nm) as well as a broad signal between 3500–3200 cm^{−1} in the corresponding DRIFTS spectrum, could be interpreted as hydrolysis of mono(oxo) dicopper sites [Cu–O–Cu]²⁺ with formation of Cu²⁺ surface hydroxyls (Eq. (8)).

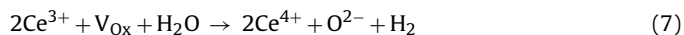
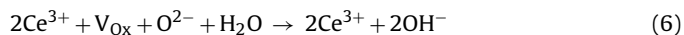


Fig. 9 compares catalytic activity in N₂O decomposition, time-based DR UV–vis profile at 588 nm (that corresponds to Ce³⁺ sites) and time-based DRIFTS profile at 3642 cm^{−1} (that corresponds to hydroxyls on CeO₂) during the *operando* step-change experiment. A clear correlation between activity drop, formation of surface ceria hydroxyl groups and decrease of Ce³⁺ surface sites can be seen. The regeneration period (5 h at 400 °C) is governed by surface dehydroxylation and formation of Ce³⁺ sites, which play a crucial role in N₂O degradation mechanism.

3.4. Proposed N₂O degradation pathway

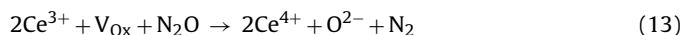
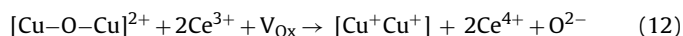
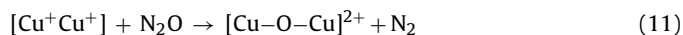
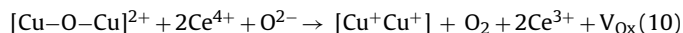
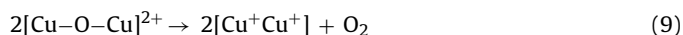
Taking into account the results of *ex situ*, *in situ* and *operando* characterizations, we can propose the N₂O decomposition mechanism over CuO/CeO₂ catalyst. Formation of mono(oxo) dicopper core species during catalyst activation and growth of DR UV–vis

peak intensity attributable to these species with increasing catalyst activity during *operando* N₂O decomposition (Fig. 3) suggest that they play a crucial role in the reaction. This is also in good agreement with the proposed mechanism of N₂O decomposition over Cu-ZSM-5 material, where participation of binuclear Cu⁺ site and mono(oxo) dicopper core in the degradation pathway was confirmed by *operando* DR UV–vis, resonance Raman and DFT calculations [33,35].

Operando UV–vis tests (Figs. 3, 7 and 9) show that the catalyst activity correlates with the absorption band of Ce³⁺ at 588 nm. In addition, *in situ* DRIFTS examination (Fig. 4) shows that labile oxygen species which participate in N₂O decomposition reaction are most probably located on CeO₂ support. Both techniques provide credible grounds that the Ce³⁺/Ce⁴⁺ redox pair importantly contributes in N₂O degradation pathway. Furthermore, CeO₂ acts like an “oxygen buffer” and has the ability to accumulate or release oxygen species.

During catalyst activation (heating in Ar to 400 °C) mono(oxo) dicopper core species are formed. The genesis of this species is accompanied with simultaneous evolution of molecular oxygen and formation of two [Cu⁺ Cu⁺] sites, which is difficult due to the necessity of oxygen recombination from two adjacent mono(oxo) dicopper sites (Eq. (9)). An alternative pathway for the formation of dimeric Cu⁺ species involves the labile oxygen from CeO₂ support (Eq. (10)). In such case, reduction of CeO₂ takes place and formation of oxygen vacancy occurs.

The catalytic cycle is initiated by the adsorption of N₂O via oxygen atom on the binuclear Cu⁺ site. Adsorption leads to weakening of N–O bond, abstraction of oxygen, N₂ desorption and generation of [Cu–O–Cu]²⁺ site (Eq. (11)).



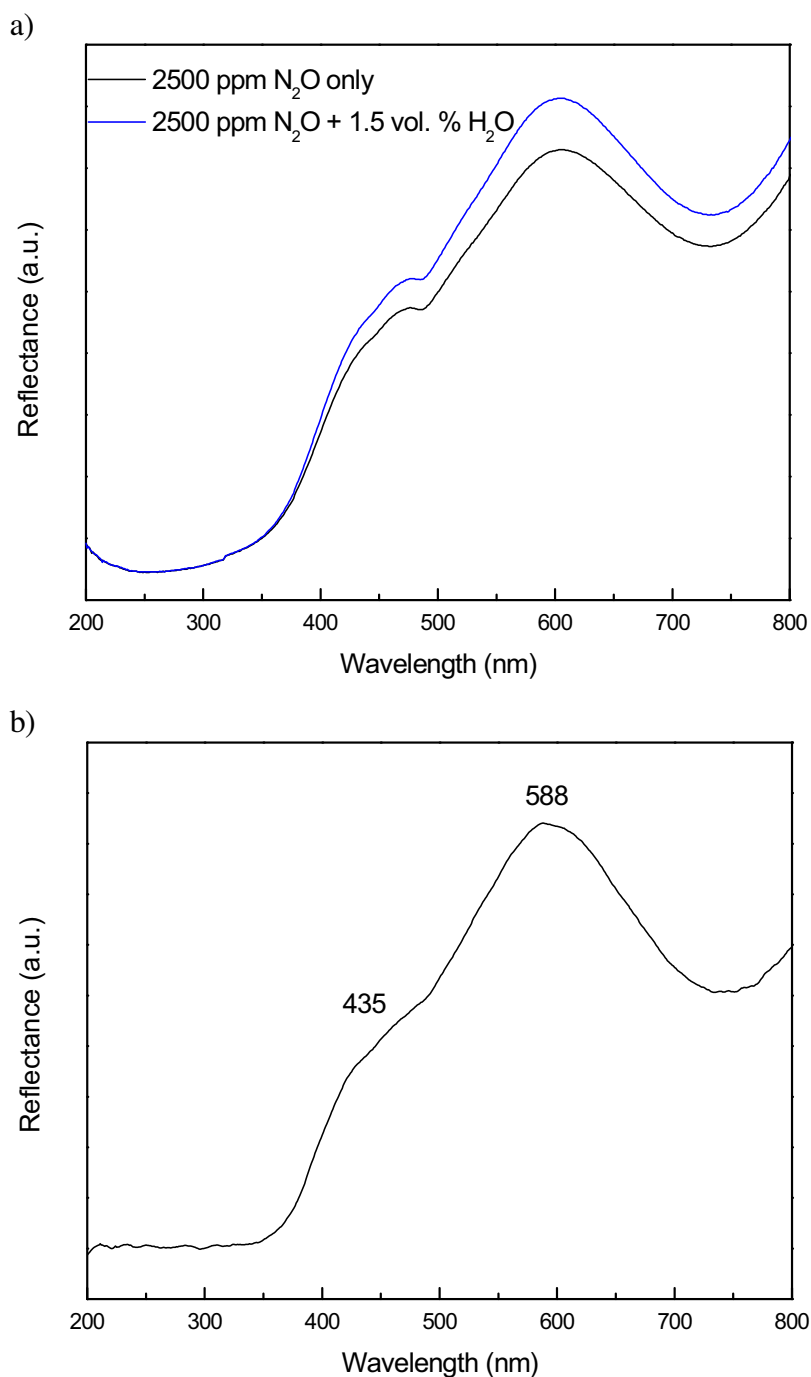


Fig. 7. Operando DR UV-vis spectra (a) of CuO/CeO₂ material during decomposition of 2500 ppm N₂O/1.5% H₂O/Ar at 400 °C, and (b) difference DR UV-vis spectrum obtained by subtraction of spectrum acquired in 2500 ppm N₂O/Ar from other spectrum.

The role of CeO₂ is not limited only to Eq. (10). Otherwise, once the source of labile oxygen is exhausted, further regeneration of binuclear Cu⁺ site with ceria contribution would be impossible. By taking into account the results of *in situ* DRIFTS examination (CeO₂ support also accumulates oxygen during N₂O decomposition reaction under low temperature, Fig. 4), we can state that the formed oxygen vacancy (Eq. (10)) further participates in catalytic pathway and can abstract oxygen either from mono(oxo) dicopper sites (Eq. (12)) or through oxygen abstraction directly from N₂O molecule (Eq. (13)). As reported previously, pure CeO₂ can decompose N₂O at 400 °C; however, its activity is low (conversion below 5%) [10]. Therefore, direct N₂O decomposition on CeO₂ (Eq. (13)) is possible,

but is not the dominant pathway. These two reactions complete the catalytic cycle and overall mechanism of N₂O degradation could be represented by Scheme 2.

Operando experiments conducted in the presence of inhibiting gases (NO and H₂O) also support the abovementioned catalytic pathway, however, the action of these two molecules is completely different. During N₂O decomposition with co-fed NO, further oxidation of the latter takes place on Cu²⁺ sites (Fig. 5). N₂O decomposition does not occur over these sites. However, during NO oxidation abstraction of labile oxygen from CeO₂ takes place (Eq. (4)). The same oxygen species also play a crucial role in Cu⁺ dimeric site regeneration, which is the active site for N₂O decomposition.

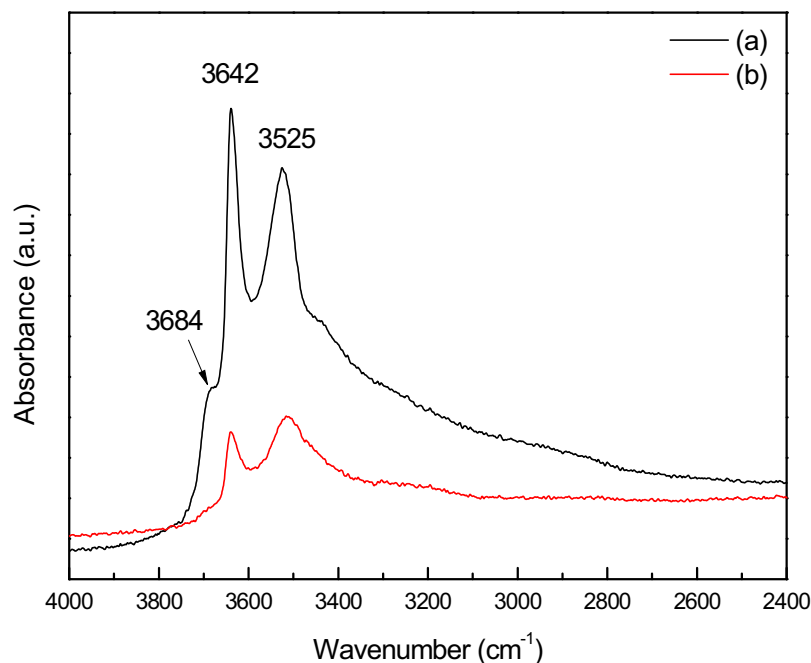


Fig. 8. *Operando* DRIFTS spectra (a) of CuO/CeO₂ material during decomposition of 2500 ppm N₂O/1.5% H₂O/Ar at 400 °C, and (b) after 20 min of catalytic reaction in 2500 ppm N₂O/Ar at 400 °C.

Therefore, oxidation of NO competes with the reaction presented in Eq. (10). The negative effect of NO does not originate from competition with the same active site, but rather from improved scavenging of oxygen species, which are required for active N₂O site regeneration. Taking into account several ways of labile oxygen replenishment (Eqs. (12) and (13)), inhibition of NO has a negative, but not crucial effect on N₂O decomposition. Thus, the resulting N₂O conversion-temperature profile is shifted to higher temperatures only for 10 °C in comparison to the experiment carried out without co-fed NO (Fig. S10).

Conversely, co-fed water vapour results in severe catalyst deactivation (Fig. S10). The presence of water vapour affects both mono(oxo) dicopper core as well as Ce³⁺ and oxygen vacancy sites, all of which participate in N₂O degradation mechanism (Fig. 7). Consequently, reoxidation of Ce³⁺ and formation of very stable hydroxyl groups occur on CeO₂ surface (treatment of at least 5 h in Ar at 400 °C is required to fully desorb H₂O and regenerate oxygen vacancies, see Fig. 9). These stable hydroxyl groups occupy positions, where labile oxygen previously resided, and thereby obstruct regeneration of Cu⁺ dimeric sites (Eq. (10)). At the same time, water also decrease the amount of mono(oxo) dicopper species (negative

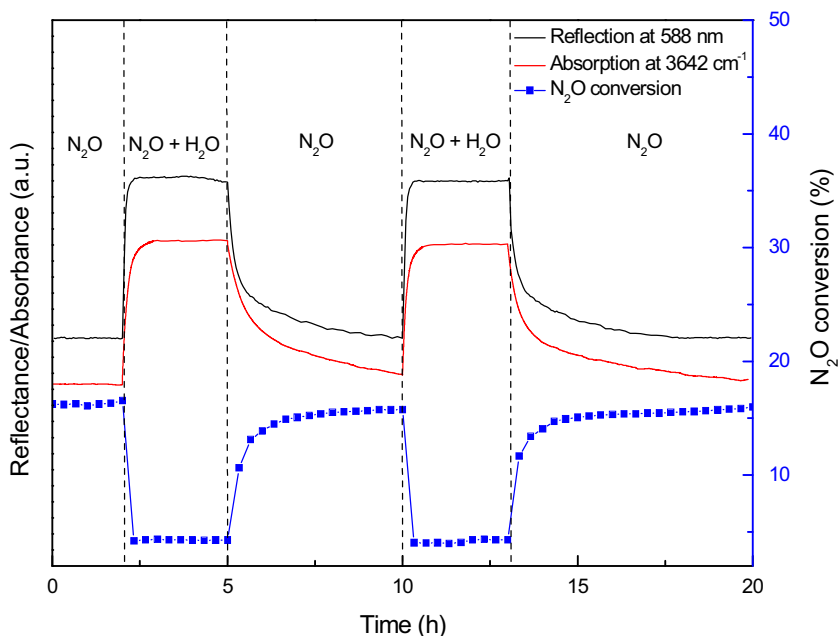
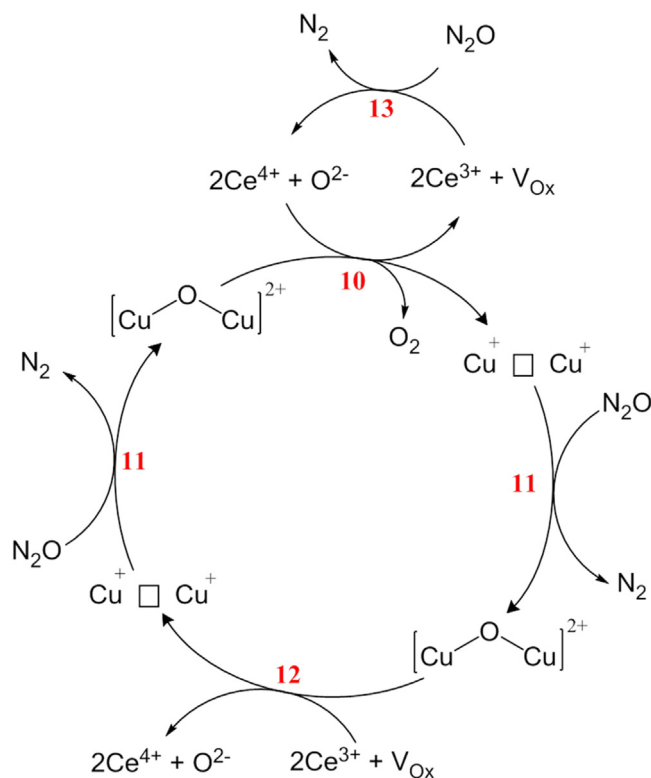


Fig. 9. Time-based *operando* DR UV-vis reflection at 588 nm, *operando* DRIFTS absorption at 3642 cm⁻¹ and N₂O conversion during change-step catalytic experiment at 400 °C (WHSV = 180 L/(g_{cat} h)).



Scheme 2. Proposed mechanism of N₂O decomposition.

peak with a maximum at 435 nm in DR UV–vis spectra (Fig. 7)) by hydrolysis of [Cu–O–Cu]²⁺ with formation of Cu²⁺ surface hydroxyls (Eq. (8)).

4. Conclusions

Based on the obtained data of *ex situ*, *in situ* and *operando* examinations, the mechanism of catalytic N₂O decomposition over CuO/CeO₂ catalyst was proposed. N₂O adsorption and further decomposition through weakening of N–O bond, abstraction of oxygen and N₂ desorption takes place on binuclear Cu⁺ sites. Formed mono(oxo)dicopper [Cu–O–Cu]²⁺ species require an additional labile oxygen atom to complete the catalytic cycle and regenerate binuclear Cu⁺ sites through molecular oxygen desorption. The predominant source of labile oxygen is located on CeO₂, therefore, the Ce³⁺/Ce⁴⁺ redox pair actively participates in active binuclear Cu⁺ site regeneration through enhanced oxygen mobility. H₂O exhibits a detrimental effect on N₂O decomposition activity and leads to shifting of the conversion-temperature profile to higher temperatures by 70 °C. Water molecules strongly and dissociatively bind to oxygen vacancy sites of CeO₂. As a result, oxygen recombination, completion of catalytic cycle and regeneration of Cu⁺ active sites are strongly hindered. On the other hand, when NO is present in the feed stream, its oxidation with labile oxygen (which participates in a key stage of O₂ desorption and active Cu⁺ site regeneration) to NO₂ takes place on the catalyst surface. Therefore, in contrast to H₂O which acts like a catalyst poison, slightly lower catalytic activity (conversion-temperature profile was shifted by 10 °C) measured in the presence of NO is a consequence of competitive oxygen consumption pathway caused by a parallel oxidation reaction. Deactivation of the CuO/CeO₂ catalyst by NO and H₂O is fully reversible at 400 °C and the initial catalytic activity can be replenished in 1 and 5 h time on stream, respectively.

Acknowledgement

The authors gratefully acknowledge the financial support of the Ministry of Education, Science and Sport of the Republic of Slovenia through Research program P2-0150.

References

- [1] D.J. Wuebbles, *Science* 326 (2009) 56–57.
- [2] A.R. Ravishankara, J.S. Daniel, R.W. Portmann, *Science* 326 (2009) 123–125.
- [3] E.A. Davidson, D. Kanter, *Environ. Res. Lett.* 9 (2014) 105012.
- [4] R. Amrousse, A. Tsutsumi, A. Bachar, *Catal. Sci. Technol.* 3 (2013) 576–579.
- [5] M. Hussain, D. Fino, N. Russo, *Chem. Eng. J.* 238 (2014) 198–205.
- [6] M. Piumetti, M. Hussain, D. Fino, N. Russo, *Appl. Catal. B Environ.* 165 (2015) 158–168.
- [7] C. Ohnishi, K. Asano, S. Iwamoto, K. Chikama, M. Inoue, *Catal. Today* 120 (2007) 145–150.
- [8] Ž. Chromčáková, L. Obalová, F. Kovanda, D. Legut, A. Titov, M. Ritz, D. Fridrichová, S. Michalik, P. Kušrowski, K. Jiráková, *Catal. Today* 257 (2015) 18–25.
- [9] T. Franken, R. Palkovits, *Appl. Catal. B Environ.* 176–177 (2015) 298–305.
- [10] M. Zabilskiy, B. Erjavec, P. Djinić, A. Pintar, *Chem. Eng. J.* 254 (2014) 153–162.
- [11] Y. Wu, C. Cordier, E. Berrier, N. Nuns, C. Dujardin, P. Granger, *Appl. Catal. B Environ.* 140–141 (2013) 151–163.
- [12] D.V. Ivanov, L.G. Pinaeva, L.A. Isupova, E.M. Sadovskaya, I.P. Prosvirnin, E.Y. Gerasimov, I.S. Yakovleva, *Appl. Catal. A: Gen.* 457 (2013) 42–51.
- [13] P. Stelmachowski, G. Maniak, J. Kaczmarczyk, F. Zasada, W. Piskorz, A. Kotarba, Z. Sojka, *Appl. Catal. B: Environ.* 146 (2014) 105–111.
- [14] G. Grzybek, P. Stelmachowski, S. Gudyka, J. Duch, K. Čmil, A. Kotarba, Z. Sojka, *Appl. Catal. B: Environ.* 168–169 (2015) 509–514.
- [15] F. Zasada, W. Piskorz, J. Janas, J. Gryboś, P. Indyka, Z. Sojka, *ACS Catal.* 5 (2015) 6879–6892.
- [16] G. Moretti, G. Fierro, G. Ferraris, G.B. Andreozzi, V. Naticchioni, *J. Catal.* 318 (2014) 1–13.
- [17] M. Rutkowska, Z. Piwowarska, E. Micek, L. Chmielarz, *Microporous Mesoporous Mater.* 209 (2015) 54–65.
- [18] P. Xie, Y. Luo, Z. Ma, C. Huang, C. Miao, Y. Yue, W. Hua, Z. Gao, *J. Catal.* 330 (2015) 311–322.
- [19] P. Xie, Y. Luo, Z. Ma, L. Wang, C. Huang, Y. Yue, W. Hua, Z. Gao, *Appl. Catal. B: Environ.* 170–171 (2015) 34–42.
- [20] M. Zabilskiy, P. Djinić, E. Tchernychova, O.P. Tkachenko, L.M. Kustov, A. Pintar, *ACS Catal.* 5 (2015) 5357–5365.
- [21] M. Zabilskiy, P. Djinić, B. Erjavec, G. Dražić, A. Pintar, *Appl. Catal. B: Environ.* 163 (2015) 113–122.
- [22] A. Adamski, W. Zajac, F. Zasada, Z. Sojka, *Catal. Today* 191 (2012) 129–133.
- [23] M.I. Konsolakis, S.A.C. Carabineiro, E. Papista, G.E. Marnellos, P.B. Tavares, J. Agostinho Moreira, Y. Romaguera-Barcelay, J.L. Figueiredo, *Catal. Sci. Technol.* 5 (2015) 3714–3727.
- [24] K. Zhou, R. Xu, X. Sun, H. Chen, Q. Tian, D. Shen, Y. Li, *Catal. Lett.* 101 (2005) 169–173.
- [25] J. Chen, Y. Zhan, J. Zhu, C. Chen, X. Lin, Q. Zheng, *Appl. Catal. A: Gen.* 377 (2010) 121–127.
- [26] J.P. Holgado, G. Munuera, J.P. Espinos, A.R. Gonzalez-Elipe, *Appl. Surf. Sci.* 158 (2000) 164–171.
- [27] A. Younis, D. Chu, S. Li, *J. Phys. D: Appl. Phys.* 45 (2012) 355101.
- [28] P.A. van Aken, B. Liebscher, *Phys. Chem. Miner.* 29 (2002) 188–200.
- [29] J. Soria, A. Martinez-Arias, J.M. Coronado, J.C. Conesa, *Top. Catal.* 11/12 (2000) 205–212.
- [30] C. Binet, A. Badri, J.-C. Lavalley, *J. Phys. Chem.* 98 (1994) 6392–6398.
- [31] H. Praliat, S. Mikhailenko, Z. Chajar, M. Primet, *Appl. Catal. B: Environ.* 16 (1998) 359–374.
- [32] S. de Tavernier, R.A. Schoonheydt, *Zeolites* 11 (1991) 155–163.
- [33] R.A. Schoonheydt, P. Vanelderen, B.F. Sels, *New and Future Developments in Catalysis. Catalysis by Nanoparticles*, in: S.L. Suib (Ed.), Elsevier B.V., 2013, pp. 399–419.
- [34] J.S. Woertink, P.J. Smeets, M.H. Groothaert, M.A. Vance, B.F. Sels, R.A. Schoonheydt, E.I. Solomon, *Proc. Natl. Acad. Sci. U. S. A.* 106 (2009) 18908–18913.
- [35] M.-L. Tsai, R.G. Hadt, P. Vanelderen, B.F. Sels, R.A. Schoonheydt, E.I. Solomon, *J. Am. Chem. Soc.* 136 (2014) 3522–3529.
- [36] C.T. Nottbohm, C. Hess, *Catal. Commun.* 22 (2012) 39–42.
- [37] M.B. Fichtl, J. Schumann, I. Kasatkin, N. Jacobsen, M. Behrens, R. Schlögl, M. Muhler, O. Hinrichsen, *Angew. Chem. Int. Ed.* 53 (2014) 7043–7047.
- [38] P. Djinić, J. Batista, A. Pintar, *Catal. Today* 147 (2009) S191–S197.
- [39] D. Gamarra, A. Martínez-Arias, *J. Catal.* 263 (2009) 189–195.
- [40] M. Manzoli, F. Menegazzo, M. Signoreto, G. Cruciani, F. Pinna, *J. Catal.* 330 (2015) 465–473.
- [41] C. Binet, M. Daturi, J.-C. Lavalley, *Catal. Today* 50 (1999) 207–225.
- [42] S. Yao, K. Mudiyanse, W. Xu, A.C. Johnston-Peck, J.C. Hanson, T. Wu, D. Stacchiola, J.A. Rodriguez, H. Zhao, K.A. Beyer, K.W. Chapman, P.J. Chupas, A. Martínez-Arias, R. Si, T.B. Bolin, W. Liu, S.D. Senanayake, *ACS Catal.* 4 (2014) 1650–1661.

- [43] R. Kydd, D. Ferri, P. Hug, J. Scott, W.Y. Teoh, R. Amal, *J. Catal.* 277 (2011) 64–71.
- [44] N. Liu, X. Chen, J. Zhang, J.W. Schwank, *Catal. Today* 258 (2015) 139–147.
- [45] K.I. Hadjiivanov, *Catal. Rev.* 42 (2000) 71–144.
- [46] A. Martínez-Arias, J.C. Conesa, J. Soria, *Res. Chem. Intermed.* 33 (2007) 775–791.
- [47] H.A. Hansen, C. Wolverton, *J. Phys. Chem. C* 118 (2014) 27402–27414.
- [48] J. Paier, C. Penschke, J. Sauer, *Chem. Rev.* 113 (2013) 3949–3985.
- [49] R.B. Duarte, O.V. Safonova, F. Krumeich, M. Makosch, J.A. van Bokhoven, *ACS Catal.* 3 (2013) 1956–1964.
- [50] D.R. Mullins, P.M. Albrecht, T.-L. Chen, F.C. Calaza, M.D. Biegalski, H.M. Christen, S.H. Overbury, *J. Phys. Chem. C* 116 (2012) 19419–19428.